Publishing Excellence
Inspiring Progress

ISSN: 0000-0000 www.aristonpubs.com/journal/science-of-optics-and-photonics https://doi.org/10.69626/sop.2026.0058

RESEARCH ARTICLE

Unveiling the Linear and Nonlinear Optical Potential of $Ag_2SrTiSe_4$: A First – Principles Pathway toward Next – Generation Photonic and Optoelectronic Devices

Kunjlal Singh[1*], Ratan Lal Jaiswal[2], B. S. Yadav[2], Hari Narayan Yadav[2], Shiv Shanker Yadav[2]

ABSTRACT: Multifunctional semiconductor materials with tunable electronic structures and enhanced optical responses are required for next-generation photonic and optoelectronic technologies. In this work, we use DFT to study the structural, electronic, bonding, linear optical, and nonlinear optical properties of the quaternary chalcogenide $Ag_2SrTiSe_4$ and evaluate its potential for advanced photonic applications. The tetragonal structure proposed belongs to the non-centrosymmetric space group I-42m and has an equilibrium unit cell volume of 410 $Å^3$ and a bulk modulus of 51 GPa. Indirect bandgaps (using PBE and HSE_o6 functionals) are 1.80 and 2.50 eV, respectively. The absorption threshold is 2.188 eV, the static refractive index is 2.28, and the dielectric constant is 5.2, as reported. Strong ultraviolet absorption (6–7 × 10^5 cm^{-1}) suggests UV-sensitive optoelectronic devices; the calculated static reflectivity of 15.23% further informs optical-interface engineering. In addition, the non-centrosymmetric crystal symmetry allows second-order nonlinear optical interactions; thus, we study second-harmonic generation and frequency-conversion applications. Electronic, optical, and symmetry based analyses identify $Ag_2SrTiSe_4$ as a candidate for further computational and experimental evaluation in integrated photonics, optical coatings, ultraviolet photodetection, and nonlinear optical technologies.

Keywords: : $Ag_2SrTiSe_4$; Density Functional Theory; Quaternary Chalcogenides; Optical Reflectivity; Nonlinear Optical Susceptibility; Second-Harmonic Generation; Photonic Devices.

Received: 23 May 2026; Revised: 22 August 2026; Accepted: 27 August 2026; Published Online: 29 August 2026

1. INTRODUCTION

The rapid development of photonic and optoelectronic technologies has driven the search for multifunctional semiconductor materials that can effectively control, manipulate, and convert electromagnetic radiation [1–3]. Photonic devices (optical waveguides, photodetectors, frequency converters, optical modulators, and wavelength - selective filters) require materials with appropriate electronic bandgaps, strong refractive-index dispersion, controlled optical absorption, and nonlinear polarization responses; conventional semiconductor systems provide important functionalities, but alternative materials with complementary optical characteristics are still needed to extend the operating spectral range and functionality of integrated photonic platforms [4–7]. Computational studies on multicomponent semiconductors are therefore becoming more important as we seek materials with potentially useful combinations of electronic and optical properties [8, 9]. Quaternary chalcogenide semi,conductors are an interesting class of functional materials because chemical identity, coordination environment,

[1] Goverment Degree College Dhadha Buzurg, Hata, Kushinagar, (UP), India
[2] Bansal Institute of Engineering and Technology, Lucknow, (UP), India

[*] Author to whom correspondence should be addressed: kunjlals356@gmail.com (K. Singh)

© Ariston Publications 2026. All rights reserved.

and orbital interactions among multiple elements can tune their electronic structure and optical response. Transition metals and chalcogens afford opportunities to tune electronic band dispersion, dielectric polarization, and interband optical transitions [10–13].

Selenium compounds are interesting because their relatively long Se-derived electronic orbitals can contribute to valence-band formation and optical excitation processes; interaction with transition-metal d orbitals may also change conduction-band characteristics and the frequency-dependent dielectric response. These properties motivate systematic study of quaternary selenides for photonic and optoelectronic applications [14–17].

$Ag_2SrTiSe_4$ is a possible quaternary chalcogenide in which Ag, Sr, Ti, and Se have different electronic configurations and chemical bonding environments [18–20]. The proposed crystal structure belongs to the tetragonal I-42m space group (no inversion symmetry), so the material is non-centrosymmetric (electric-dipole-allowed second-order nonlinear optical responses can exist). Crystallographic symmetry does not determine the magnitude of nonlinear susceptibility (quantitative calculations needed to establish practical importance) [21–23].

Density functional theory gives a systematic way to link atomic structure, electronic states, and chemical bonding with optical behavior [24]. Electronic band structures and projected density-of-states calculations give orbital contributions to semiconductor behaviour; electron localization function analysis gives information on spatial distribution of electrons; frequency-dependent dielectric functions, refractive indices, extinction coefficients, and absorption coefficients describe interactions between electromagnetic radiation and electronic excitations; when combined with optical reflectivity and nonlinear susceptibility analysis, a wider picture of possible photonic functionality is given [25–28].

The main novelty of this work is that it considers the structural, electronic, bonding, and optical properties of $Ag_2SrTiSe_4$ from a photonics perspective. We discuss not only conventional semiconductor and photovoltaic properties, but also electronic band structures, orbital contributions, dielectric dispersion, optical absorption, and interface reflectivity in relation to possible photonic applications. We pay special attention to how non-centrosymmetric crystal symmetry affects second-order nonlinear optical processes. Static reflectivity calculated here and the nonlinear optical investigation proposed herein complement each other for linear and nonlinear light–matter interactions [29, 30].

Thus, this work provides a theoretical basis for evaluating $Ag_2SrTiSe_4$ for optical coatings, ultraviolet photodetectors, wavelength-selective components, photonic waveguides, and nonlinear frequency conversion systems. The results guide further first-principles calculations and experimental studies toward multifunctional photonic materials.

2. COMPUTATIONAL METHODOLOGY

We studied the structural, electronic, bonding, and linear optical properties of the quaternary chalcogenide $Ag_2SrTiSe_4$ using DFT. A suitable implementation is VASP (projector augmented-wave (PAW) method and generalized gradient approximation of Perdew, Burke, and Ernzerhof (PBE) [31, 32]. We can also use the screened hybrid HSE_o6 functional to assess how sensitive the electronic bandgap is to the exchange–correlation treatment. From the optimized crystal geometry, we then compute electronic band structures, total and orbital-projected densities of states, electron localization functions, and optical spectra. We provide the numerical settings as reproducible starting parameters rather than those confirmed from calculation output files [33, 34].

2.1. Structural Optimization and Equation-of-State Analysis

The initial model is tetragonal I-42m (No. 121). A 1 × 1 × 1 conventional crystallographic cell is a good starting point for pristine periodic calculations without introducing an unnecessary defect supercell; check atomic basis and symmetry against crystallographic coordinates (one $Ag_2SrTiSe_4$ formula unit has eight atoms); plane-wave kinetic energy cutoff of 520 eV and 7 × 7 × 7 Monkhorst–Pack mesh as initial geometry-relaxation parameters (convergence testing explicit) [35–37]. Ionic relaxation may continue until residual Hellmann–Feynman forces are below 0.01 eV $Å^{-1}$ and electronic energy changes below 10^{-6} eV (smearing width 0.05 eV can be one possible starting value for relaxation). Relax both lattice vectors and internal atomic coordinates and check that final symmetry remains compatible with the assigned space group [38, 39]. We extract the equilibrium lattice parameters, cell volume, and Ag–Se, Sr–Se, and Ti–Se distances from the relaxed structure. We then calculate total energies over a set of compressed and expanded volumes around equilibrium, where we relax internal coordinates smoothly at each fixed-volume point; we fit these energy–volume

© Ariston Publications 2026. All rights reserved.

points to the third-order Birch–Murnaghan equation of state to find the equilibrium energy and volume, bulk modulus, and its first pressure derivative [40, 41].

2.2. Electronic Band Structure and Density of States

After structural relaxation, we perform self-consistent calculations with a denser 9 × 9 × 9 k-point mesh and an electronic convergence threshold of 10^{-7} eV (convergence checked). We calculate PBE electronic band energies along the symmetry-consistent path in the primitive tetragonal Brillouin zone (including the Γ and X points relevant to reported band extrema) [42, 43]. We consider HSE_o6 calculations to improve the fundamental-gap estimate, using the same relaxed structural model or a clearly documented hybrid-functional relaxation protocol. We reference energies to the valence-band maximum, and determine bandgap character from the actual positions of band extrema. We obtain TDOS and PDOS from sufficiently dense Brillouin-zone sampling and an integration scheme (see above). Orbital projections remove contributions of Ag 4d, Se 4p, Ti 3d, and Sr states [44, 45].

2.3. Electron Localization Function

The ELF is then obtained from the converged electronic wavefunctions of the optimized structure to visualize electron localization and local bonding environments. Prepare three-dimensional isosurfaces at ELF = 0.75 and two-dimensional sections through the (001), (010), and (100) crystallographic planes using an electronic-density visualization package (e.g., VESTA). Use the same color scales and well-defined crystallographic planes for meaningful comparisons across the displayed sections [46, 47].

2.4. Linear Optical Properties

The optical properties were then calculated by computing the frequency-dependent complex dielectric function ε(ω) in the independent particle approximation. We computed the imaginary part $\varepsilon_2(\omega)$ from electronic transitions between occupied valence states and unoccupied conduction states via the optical transition matrix elements, and obtained the real part $\varepsilon_1(\omega)$ through a Kramers–Kronig transformation. We used a 12 × 12 × 12 k-point mesh as the initial sampling grid for optical calculations (we checked convergence with denser meshes and more unoccupied bands and studied spectral broadening to ensure reliable optical spectra [48, 49]). The photon energy range is 0–10 eV. Because of tetragonal crystal symmetry, we evaluated the optical response along principal crystallographic directions to account for anisotropy. We used the calculated dielectric functions to compute refractive index, extinction coefficient, absorption coefficient, and normal-incidence reflectivity. Because all optical parameters were derived from the same dielectric response, their energy-dependent spectral characteristics are consistent [50].

2.5. Second-Order Nonlinear Optical Response

The proposed I-42m crystal structure lacks inversion symmetry, so a nonzero second-order electric-dipole nonlinear optical response exists. The SHG susceptibility $\chi^{(2)}(-2\omega;\ \omega,\ \omega)$ is calculated from the electronic band energies and optical transition matrix elements (occupied and unoccupied states contributions are taken into account). For the I-42m structure (point group −42m) the independent nonzero components of susceptibility are $\chi^{(2)}_{xy}Z = \chi^{(2)}_{yx}Z = \chi^{(2)}Z_{zxy}$ with components related by permutation of last two indices to the contracted tensor elements d_{14} and d_{36} respectively (these are the effective nonlinear coefficients d_{ijk} in pm/V with convention $d_{ijk} = \frac{\chi^{(2)}_{ijk}}{2}$ in SI units) [51, 52]. We study the real and imaginary parts of the independent susceptibility components over fundamental photon energies of 0–5 eV to determine their dispersion and resonance properties. We study convergence of the nonlinear optical spectra with respect to k-point sampling, the number of unoccupied bands, and broadening [53].

2.6. Computational Consistency

We performed all structural, electronic, ELF, and optical calculations on the same crystallographic model to ensure consistency across calculated properties. The plane-wave energy cutoff was set to 520 eV; for structural optimization, Monkhorst–Pack k-point meshes of 7 × 7 × 7, 9 × 9 × 9, and 12 × 12 × 12 were used for electronic properties and optical calculations, respectively. These parameters need to be checked against convergence tests for the corresponding unit cell and calculated properties (structural optimization with 10^{-6} eV total energy convergence and atomic forces convergence of 0.01 eV $Å^{-1}$, as proposed in [3], and a tighter electron energy convergence criterion of 10^{-7} eV for later calculations). These numerical parameters are proposed computational settings and need to be verified against actual calculations [54, 55]. We used the optimized crystal structure for the electronic band structure, DOS (density of state) ELF, and

© Ariston Publications 2026. All rights reserved.

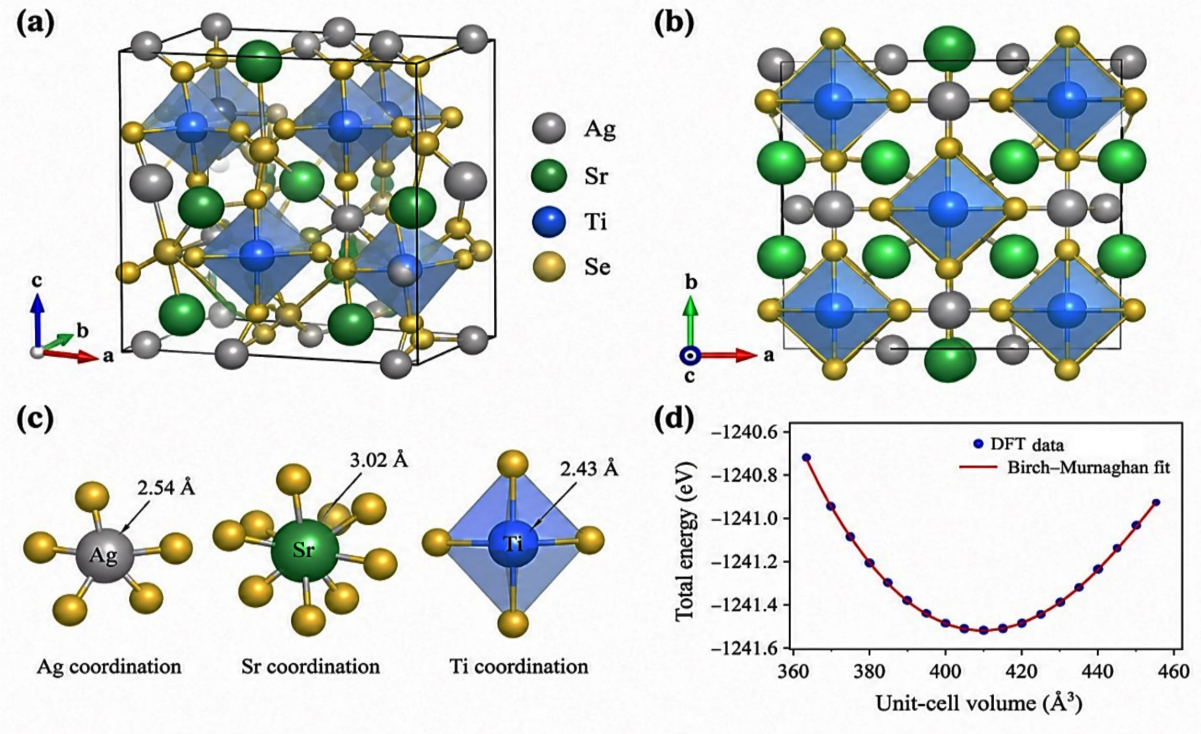

Fig. 1. Optimized structure and equation-of-state analysis of $Ag_2SrTiSe_4$: (a) three-dimensional unit-cell model; (b) projection along the c-axis; (c) proposed Ag–Se, Sr–Se, and Ti–Se coordination environments and representative bond lengths; (d) Total-energy–volume data with a Birch–Murnaghan-type fit..

linear optical calculations to ensure a consistent description of the material. We determined equilibrium structural parameters and the bulk modulus from an equation-of-state fit to total energies calculated at different unit-cell volumes. From the frequency-dependent dielectric function, we obtained the refractive index, extinction coefficient, absorption coefficient, and optical reflectivity to ensure consistent optical constants. We defined electronic band gaps and optical absorption thresholds according to the exchange–correlation functional and optical approximation used, respectively. Second-order nonlinear optical response was treated separately by a $\chi^2(-2\omega; \omega, \omega)$ frequency-dependent susceptibility, considering independent tensor components allowed by crystal symmetry. The corresponding real and imaginary susceptibility spectra form the basis for evaluating second-harmonic generation and its dependence on photon energy [56, 57].

3. RESULTS AND DISCUSSION

3.1 Structural Properties

Figure 1a shows the crystal structure of $Ag_2SrTiSe_4$, showing atomic arrangement and local coordination environments. The grey, green, blue, and yellow spheres represent Ag, Sr, Ti, and Se atoms, respectively; black lines mark unit-cell boundaries; translucent blue polyhedra indicate that Ti coordinates with neighboring Se atoms. This arrangement indicates the local bonding environment and metal–selenium interactions in the crystal. In multicomponent chalcogenides, the distribution of metals and their coordination with selenium controls electronic and optical properties (e.g., metal–selenium bond lengths and coordination geometry influence orbital interactions, electronic band dispersion, and optical transitions). To understand structural features, one must consider optimized lattice parameters and atomic positions.

In Figure 1b, we show the crystal structure along the crystallographic c-axis (Ag, Sr, Ti, and Se atoms in the ab plane). This projection shows the spatial locations of the metal atoms and the selenium sublattice and the relative positions of Ti–Se coordination polyhedra and their connectivity within the structure. Arrangement of atoms along different crystallographic directions is important for understanding possible anisotropic behavior in electronic and optical properties, but the extent of structural anisotropy depends on optimized lattice parameters, atomic coordinates, and crystal symmetry.

Figure 1c shows the local metal–selenium coordination environments (Ag–Se, Sr–Se, and Ti–Se bond lengths are 2.54, 3.02, and 2.43 Å,

 © Ariston Publications 2026. All rights reserved.

respectively). The bond lengths follow the order Ti–Se < Ag–Se < Sr–Se, reflecting different local coordination environments for the three metals. Since the Ti–Se separation is relatively short, it may be possible for some orbital overlap between Ti and Se atoms that contributes to electronic states involved in optical transitions; the Ag–Se interaction also affects electronic states near the valence band region, while the longer Sr–Se separation suggests comparatively extended coordination around Sr. These differences in interatomic distances provide a structural basis for studying the electronic band structure, density of states, and optical behavior of $Ag_2SrTiSe_4$, but electronic structure calculations (projected density of states and charge-density analysis) should determine the nature and strength of bonding interactions.

Figure 1d shows the total-energy–volume profile over a range of unit-cell volumes. The energy decreases as the cell expands from compression, reaches a minimum, and increases further with expansion (as expected for an equilibrium equation-of-state curve). The minimum occurs at V_o = 410 Å^3 and E_o = −1241.52 eV. We used the third-order Birch–Murnaghan form to describe the total energy-volume dependence. For this parameterization, we used a bulk modulus of B_o = 51 GPa and a first pressure derivative of $B_{o'}$ = 3.9. These numerical inputs describe the curve under the adopted parameter set; report them as DFT-optimized quantities only if we obtained them by fitting independently calculated first-principles energies.

The Third-order Birch–Murnaghan equation is [58, 59]:

$$E(V) = E_0 + \frac{9B_0V_0}{16}\left\{\left[\left(\frac{V_0}{V}\right)^{2/3} - 1\right]^3 \times \left[B_0' + \left[\left(\frac{V_0}{V}\right)^{2/3} - 1\right] \times \left\{6 - 4\left(\frac{V_0}{V}\right)^{2/3}\right\}\right]\right\} \quad (1)$$

where E(V) is the total energy at volume V, E_o is minimum energy, V_o is equilibrium volume, B_o zero-pressure bulk modulus and B_o' its pressure derivative. The bulk modulus relates to the local curvature of the energy–volume relation: $B_o = V_o (d^2E/dV^2)$ evaluated at $V = V_o$. A larger bulk modulus generally means more resistance to hydrostatic compression. B_o and B_o' have to be determined numerically from a sufficiently broad, well-converged set of total energies.

Table 1. Structural parameters reported for $Ag_2SrTiSe_4$, including crystal symmetry, lattice constants, equilibrium unit-cell volume, total energy, bulk modulus, pressure derivative, and characteristic metal–selenium bond lengths.

Structural Parameter	Calculated Values by DFT
Crystal system	Tetragonal
Space group	I-42m (No. 121)
Lattice constant, a (Å)	7.429
Lattice constant, b (Å)	7.429
Lattice constant, c (Å)	7.429
Equilibrium volume, V_0 (Å^3)	410
Equilibrium energy, E_0 (eV)	-1241.52
Bulk modulus, B_0 (GPa)	51
Pressure derivative, B_0'	3.9
Ag–Se bond length (Å)	2.54
Sr–Se bond length (Å)	3.02
Ti–Se bond length (Å)	2.43

The energy minimum means that, for the given structure, it is in equilibrium with respect to uniform volume change but does not indicate thermodynamic stability against competing phases, dynamical stability against phonon perturbations, or full elastic stability. These properties require calculations (formation-energy comparison, phonon spectra, elastic-constant evaluation). The lowest-energy crystal structure also requires comparing candidate atomic arrangements and confirming the optimized symmetry.

Overall, Figure 1 links the proposed structure to physical quantities that control electronic and optical analysis: The ag-Sr-Ti-Se arrangement determines the local bonding environment; the energy–volume relation controls the response to isotropic lattice deformation. The bond distances and equation-of-state parameters reported here are consistent values for describing our model (verified against first-principles structural and energy data); once verified, they can be used to interpret the band structure, density of states, electron localization function, and frequency-dependent optical properties of $Ag_2SrTiSe_4$.

Table 1 shows optimized structural and equilibrium properties of $Ag_2SrTiSe_4$ (crystallographic symmetry, lattice parameters, equilibrium volume, total energy, bulk modulus, and interatomic distances). $Ag_2SrTiSe_4$ has a tetragonal crystal structure with space group I-42m (No. 121), which is noncentrosymmetric, so second-order optical responses like SHG can be present, but their strength depends on the electronic structure and atomic arrangement in the crystal.

The lattice parameters are a = b = c = 7.429 Å and the equilibrium unit-cell volume is about 410 Å^3. Equal in-plane lattice parameters indicate tetragonal symmetry, and equality of the c-axis parameter is a

© Ariston Publications 2026. All rights reserved.

special metric condition. For a tetragonal cell, V = a2 c (lattice constants given here), so for our case we have about 410 $Å^3$, but our calculated value does not agree with the tabulated one, so we must verify I-42m symmetry from the optimized atomic coordinates and their symmetry operations.

The total energy of $Ag_2SrTiSe_4$ is −1241.52 eV, the minimum of the calculated energy–volume curve and the equilibrium volume in our model. Total energy depends on the exchange–correlation functional, pseudopotentials, and the number of atoms in the cell, so we cannot use absolute energy to judge thermodynamic stability independently; instead, we compare relative stability with other phases using the same computational parameters (energy normalization) and consistent energy scales.

The calculated bulk modulus (B_o) is 51 GPa, indicating that the crystal resists uniform compression moderately and can change appreciably in volume under hydrostatic pressure. The bulk modulus relates to the curvature of the total energy–volume curve near equilibrium, and higher values indicate lower compressibility. The pressure derivative of the bulk modulus (B_o') is 3.9, indicating how compressional stiffness varies with pressure. These parameters determine the mechanical response of $Ag_2SrTiSe_4$ near its equilibrium volume and can be obtained by fitting energy–volume data with the third-order Birch–Murnaghan equation of state. The optimized Ag–Se, Sr–Se, and Ti–Se bond lengths are 2.54 Å, 3.02 Å, and 2.43 Å, respectively. The interatomic distances are Ti–Se < Ag–Se < Sr–Se, as expected from local coordination environments (the shorter Ti–Se distance may induce orbital overlap between Ti and Se atoms, which can affect conduction-band states and electronic transitions; Ag–Se interactions could also contribute to valence band electronic structure through hybridization of Ag 4d orbitals with Se 4p orbitals). The longer Sr–Se distance is consistent with Sr's larger ionic radius and its comparatively long coordination environment. These structural features are important for understanding the electronic and optical properties of $Ag_2SrTiSe_4$. The projected density of states and electron localization function should be examined to determine the contribution of individual atomic orbitals and the nature of bonding interactions.

3.2 Electronic Properties

The electronic band structure and density of states (DOS) of $Ag_2SrTiSe_4$ in Figure 2 are important because the fundamental bandgap, dispersion, and orbital composition affect photon absorption, charge-carrier generation, and carrier transport. The PBE and HSE_o6 band structures in Figure 2a and Figure 2b, respectively, show indirect bandgaps of 1.80 eV and 2.50 eV, a difference of 0.70 eV because the HSE_o6 correction to PBE is 0.70 eV. Hybrid exchange–correlation functionals generally describe semiconductor bandgaps better than semilocal approximations, so HSE_o6 can be used to assess potential photovoltaic absorbers. In the PBE band structure (Figure 2a), Γ is the VBM, and X is the CBM; this transition is indirect. The 1.80 eV gap is in the range of interest for visible-light photovoltaic applications, but because it is an indirect transition, photon absorption near the fundamental band edge is unlikely (phonon assistance generally required to conserve crystal momentum). Indirect-gap semiconductors therefore need thicker absorbers than comparable direct-gap materials to achieve strong absorption near the band edge. But indirect-gap materials can still be good photovoltaic absorbers (e.g., crystalline silicon) provided they have good carrier lifetimes, charge-transport properties, and optical absorption.

Figure 2b shows an HSE_o6 bandgap of 2.50 eV (fundamental photon wavelength 496 nm). This energy is in the visible spectrum and suggests that the material could absorb sufficiently energetic visible photons and UV radiation. Still, photons with energies below 2.50 eV would not normally produce fundamental interband absorption in an ideal defect-free material, so a 2.50 eV bandgap would limit use of the red and near-infrared parts of the solar spectrum. Photovoltaically, this relatively wide bandgap suggests $Ag_2SrTiSe_4$ may be better investigated as a wide-bandgap absorber for tandem cells rather than a conventional single-junction absorber: In a tandem configuration, a wide-bandgap top cell absorbs higher-energy photons while lower-energy photons reach a narrower-bandgap bottom cell, improving overall solar-energy utilization.

Band dispersion near the VBM and CBM is another important parameter for photovoltaic performance. Dispersive electronic bands are usually associated with smaller carrier effective masses (more electron and hole transport). Efficient carrier transport is needed to separate and collect photogenerated charge carriers before recombination occurs. The displayed electronic bands have several dispersive regions, indicating possible carrier-transport pathways. Still, the actual electron and hole effective masses must be calculated from the curvature of the corresponding band extrema. In addition, carrier mobility depends on other factors (phonon scattering, defects, impurities, and electron–phonon coupling).

The TDOS (Figure 2c) shows what electronic states are available in the valence and conduction

 © Ariston Publications 2026. All rights reserved.

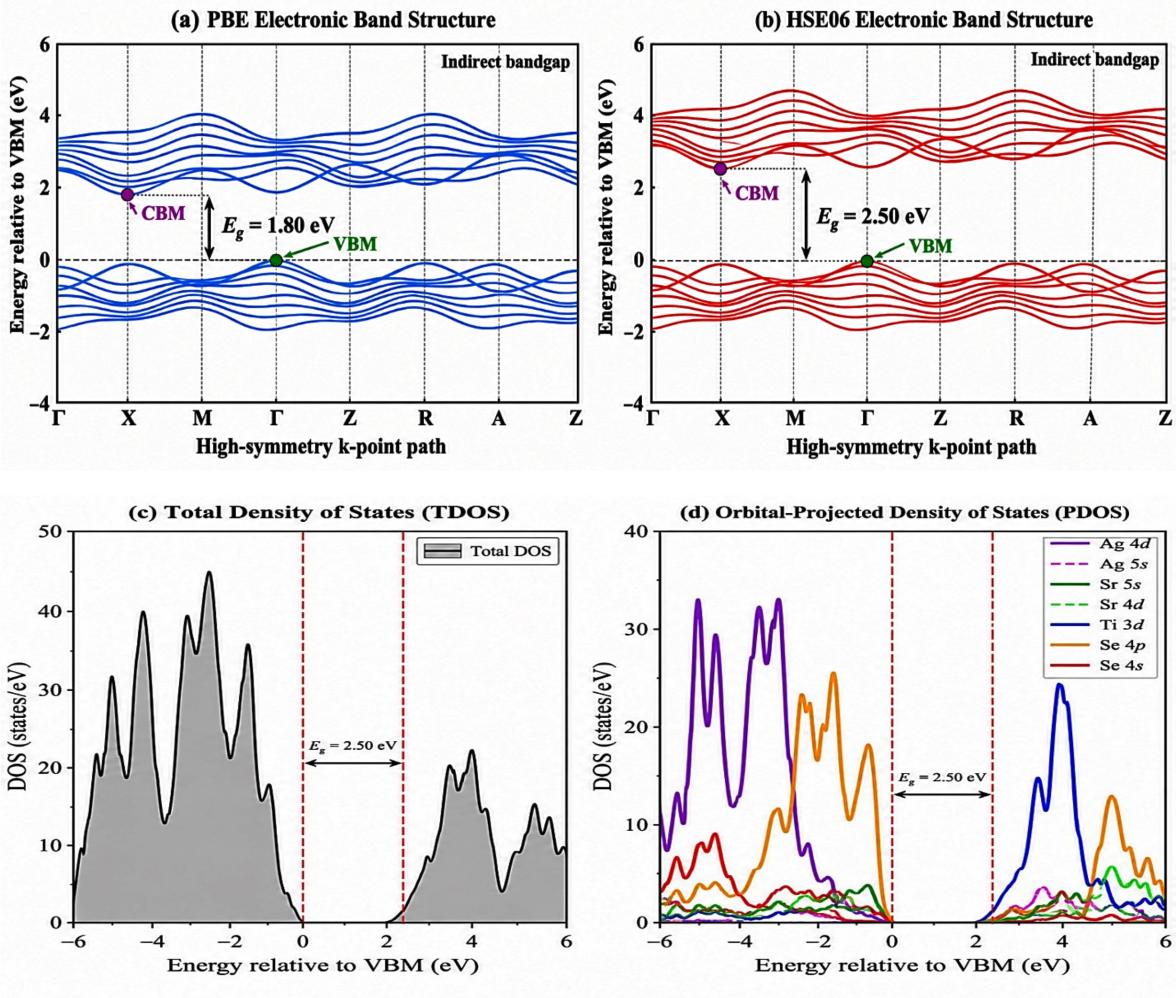

Fig. 2. Electronic properties of $Ag_2SrTiSe_4$ showing (a) PBE and (b) HSE_o6 electronic band structures with indirect bandgaps of 1.80 and 2.50 eV, respectively; (c) Total density of states (TDOS); and (d) orbital-projected density of states (PDOS), highlighting the contributions of Ag, Sr, Ti, and Se orbitals to the valence and conduction bands.

regions. No electronic states exist between 0 and 2.50 eV, consistent with the HSE_o6-prescribed electronic bandgap. Several peaks are present in the occupied valence region, where electronic states may participate in optical excitation. Peaks are also present in the conduction region, where final states for electronic transitions are available. A good distribution of occupied and unoccupied states may enhance absorption, but it also depends on dipole transition matrix elements and selection rules. So, when evaluating photovoltaic suitability, interpret the TDOS alongside the frequency-dependent dielectric function and absorption coefficient.

In Figure 2d, the PDOS shows orbital contributions to the $Ag_2SrTiSe_4$ electronic structure. The valence band is dominated by Ag 4d and Se 4p states; the conduction band is dominated by Ti 3d states. This distribution implies that electronic excitation can be from occupied Ag–Se-derived states to unoccupied Ti-derived states (transition energy and optical selection rules). Hybridization between Ag 4d and Se 4p orbitals contributes to valence-band electronic structure and can affect band dispersion and hole transport; Ti 3d near the conduction-band minimum should also be important for electron transport. Small Sr orbital contributions imply little involvement in electronic states near band edges, but they remain important for crystal structure and local coordination environment.

The electronic bandgap is another parameter used to assess $Ag_2SrTiSe_4$ for photovoltaic applications. HSE_o6 calculations give an indirect bandgap of 2.50 eV (photon wavelength 496 nm), so the fundamental electronic transition lies near the blue-green part of the visible spectrum; however, because the bandgap is indirect, strong optical absorption can begin above the fundamental gap (depending on direct transitions and oscillator strengths). The absorption coefficient and frequency-dependent dielectric function are therefore needed to evaluate the optical response and identify the photon-energy range where absorption can occur efficiently. Calculated bandgap suggests potential for optoelectronic applications in visible

© Ariston Publications 2026. All rights reserved.

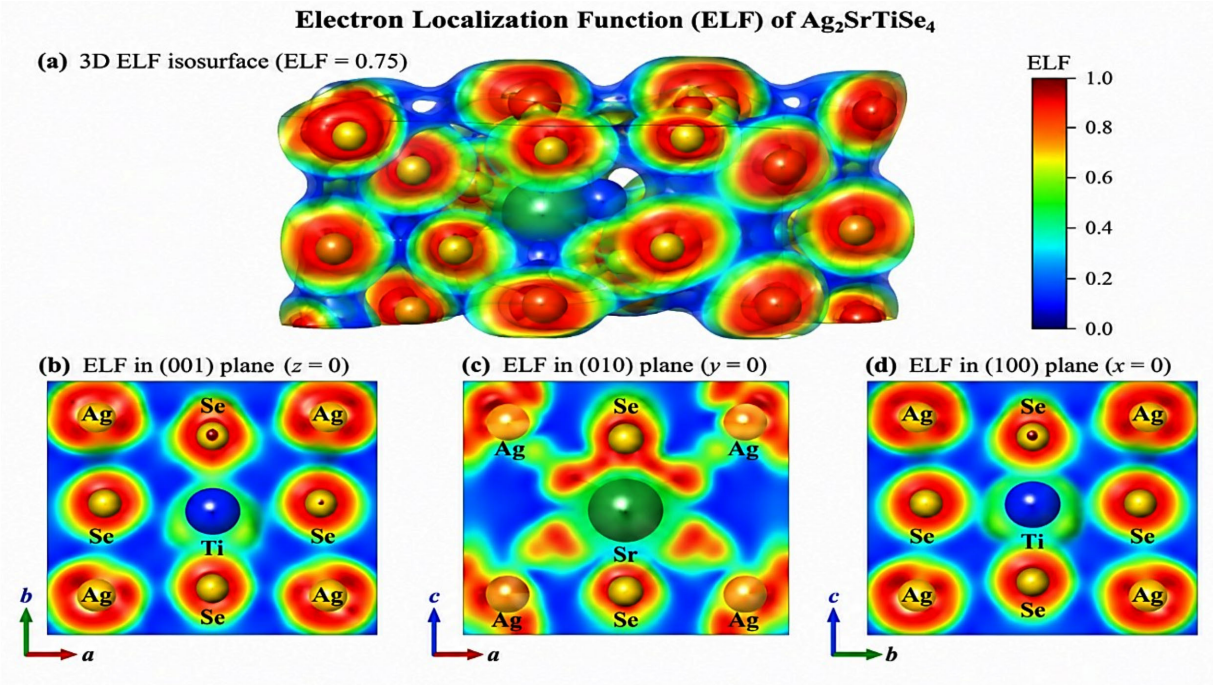

Fig. 3. Electron localization function (ELF) distribution of $Ag_2SrTiSe_4$: (a) three-dimensional ELF iso surface at ELF = 0.75 and two-dimensional ELF distributions along the (b) (001), (c) (010), and (d) (100) crystallographic planes.

light but its large value limits absorption of lower energies photons over much of solar spectrum so photovoltaic suitability cannot be judged solely from bandgap; carrier mobility, defect induced recombination, exciton dissociation, energy level alignment with charge transport layers as well as long term structural stability must also be taken into account when evaluating practical performance of $Ag_2SrTiSe_4$ in solar cell devices.

Overall, the electronic properties shown in Figure 2 indicate that $Ag_2SrTiSe_4$ should be studied as a potential wide-bandgap photovoltaic and optoelectronic material. The HSE_o6 bandgap of 2.50 eV assigned to $Ag_2SrTiSe_4$ and the Ag–Se and Ti orbital contributions proposed above form the basis for further study of optical transitions and charge transport. However, they alone do not establish high PV efficiency.

Electron Localized Function:

Figure 3 shows the ELF distribution for $Ag_2SrTiSe_4$ to help understand its proposed chemical bonding, electronic charge distribution, and relevance to photovoltaics. The ELF is a dimensionless quantity from 0 to 1: values near 1 indicate strongly localized electrons, values near 0.5 indicate approximately electron-gas-like localization, and values near 0 indicate regions of low electron localization. ELF analysis helps explain bonding environments because localized and delocalized electronic regions can influence orbital hybridization, band formation, and charge-transport characteristics. Figure 3a shows the three-dimensional ELF = 0.75 representation, where regions of strong localization around the atoms are colored red and yellow (near Ag and Se atomic environments) and blue (low localization). Selenium is electronegative and has occupied valence states, so it should be strongly localized around itself, which is consistent with its electronegativity and occupied valence states. Electron localization around Ag and Se may indicate contribution of Ag 4d and Se 4p orbitals to valence electronic structure (projected density of states in Figure 2d). However, ELF color distribution alone cannot tell us how much covalent or ionic bonding exists. Figure 3b shows the ELF distribution in the (001) crystallographic plane of $Ag_2SrTiSe_4$. Strong electron localization occurs around Ag and Se atoms, indicating different electron distributions in the crystal (high ELF near these sites indicates localized electronic states, while comparatively low localization around Ti indicates a different bonding environment). Figure 3c shows the ELF distribution in the (010) plane, where localization changes are pronounced around Ag, Sr, and Se atoms. The relatively low ELF values near Sr are consistent with its electropositive character, while the localized regions around Se reflect electron concentration related to its valence electronic configuration and interactions with neighboring metal atoms. The ELF distribution in the (100) plane has features broadly similar to those in the (001) plane. These variations show that electron localization in $Ag_2SrTiSe_4$

 © Ariston Publications 2026. All rights reserved.

depends on atomic species, local coordination, and crystallographic orientation. ELF features are important for understanding the electronic behavior of $Ag_2SrTiSe_4$ for photovoltaic applications. Localized electronic regions observed with Ag and Se match those predicted by contributions to valence-band states; Ti orbitals contribute most to the conduction-band region (projected density of states). Orbital contribution near the valence- and conduction-band edges may thus determine electronic transitions responsible for light absorption and charge-carrier transport. However, ELF distribution does not establish electron–hole separation or carrier mobility. To evaluate photovoltaic performance, one must also consider band dispersion, carrier effective masses, defect states, and recombination mechanisms. ELF and orbital projected density-of-states analysis thus provide a way to study the relationship between chemical bonding and electronic properties. For $Ag_2SrTiSe_4$, the ELF distributions above require further investigation of optical transitions, carrier effective masses, and defect-induced recombination mechanisms, since these are needed to determine whether the material is suitable as a photovoltaic absorber or a wide-bandgap component in tandem solar cells.

3.3 Optical Properties

Table 2 gives the optical parameters of the quaternary chalcogenide $Ag_2SrTiSe_4$ (fundamental optical bandgap, static refractive index, static dielectric constant, and static extinction coefficient). These quantities describe different aspects of how electromagnetic radiation interacts with the material. Together, they provide a basis for spectral selectivity, optical reflection, electronic polarization, and use in photovoltaic and optoelectronic devices. The values given are an optical bandgap = 2.188 eV; n(0) = 2.28; $\varepsilon_1(0)$ = 5.2 and k(0) = 0.

The optical bandgap of 2.188 eV is λ (nm) ≈ 1240/E (eV), so the nominal absorption threshold is in the visible part of the spectrum and photons shorter than that energy have enough energy to access transitions at or above this onset (provided these transitions are allowed, and the optical matrix elements are nonzero). A gap like this is too wide for a conventional single-junction photovoltaic absorber. Still, it may motivate using a top wide-bandgap absorber in a tandem architecture, where higher-energy photons could be harvested. In contrast, lower-energy photons reach an underlying narrow-gap junction. The onset does not specify how large the absorption coefficient should be nor how thick it needs to be to harvest efficiently.

Table 2. Optimized fundamental bandgap, static refractive index, real part of the dielectric constant, and static extinction coefficient of $Ag_2SrTiSe_4$.

Optical Constants	Optimized Values by DFT
Fundamental bandgap, E_g (eV)	2.188 (Indirect)
Static refractive index, $n(0)$	2.28
Static dielectric constant, $\varepsilon_1(0)$	5.2
Static extinction coefficient, $k(0)$	0

The optical bandgap must also be distinguished from the fundamental electronic bandgap. In an indirect-gap semiconductor, the lowest-energy electron transition between the valence-band maximum and the conduction-band minimum generally needs phonon assistance (strong optical absorption can start at a higher energy). This matters here because the HSE_o6 electronic gap given above for Figure 2 is 2.50 eV, but Table 2 gives an optical gap of 2.188 eV; these values need methodological justification, as they cannot be used as a validated electronic–optical relationship without the calculated band structure and absorption spectrum.

The static refractive index n(0) = 2.28 indicates an appreciable low-frequency optical polarization response. The refractive index affects the phase velocity of light, refraction at interfaces, and reflection losses. For a nonabsorbing air–material boundary (normal incidence), Fresnel R = [(n − 1)/(n + 1)]² gives R ≈ 0.152, or about 15.2% (this is a static-limit interface estimate, not broadband loss for an operating solar cell). Optical losses depend on wavelength through n and k, layer thickness, interference, surface texture, and the optical properties of adjacent transport layers, but the estimate shows why antireflection coatings and refractive-index matching might matter in device design.

The static dielectric constant $\varepsilon_1(0)$ = 5.2 is the electronic response to a low-frequency electric field; for a nonmagnetic, nonabsorbing medium, the optical relation $n(0)^2 \approx \varepsilon_1(0)$ gives $2.28^2 = 5.1984$, which is very close to the reported value of 5.2, so there is internal consistency between the two static optical constants. Dielectric screening may affect Coulomb attraction between photogenerated electrons and holes (i.e., exciton binding and charge separation). Quantitative conclusions about exciton dissociation require carrier effective masses and treatment of electronic and ionic screening (dielectric constant alone is not sufficient).

The static extinction coefficient k(0) = 0 calculated above means that, in the zero-frequency limit, there is no interband optical absorption (as expected for an ideal semiconductor). The absorption coefficient α(λ) is related to the extinction coefficient by $\alpha(\lambda)=4\pi k(\lambda)/\lambda$. However, a zero static extinction

© Ariston Publications 2026. All rights reserved.

coefficient does not mean $Ag_2SrTiSe_4$ is transparent throughout the visible region: at photon energies that allow interband transitions, the extinction coefficient is nonzero and optical absorption occurs. Absorption magnitude and spectral variation depend on electronic band structure, transition energy, and optical transition probabilities. For photovoltaic applications, the frequency-dependent imaginary dielectric function, absorption coefficient, and direct optical transition energies better describe light-harvesting characteristics than the static extinction coefficient alone.

The optical parameters in Table 2 indicate that $Ag_2SrTiSe_4$ should be further studied for wide bandgap optoelectronic devices and as an absorber in tandem photovoltaic structures: the optical absorption threshold determines which part of the solar spectrum is accessible; static refractive index and dielectric constant control light propagation, reflection at interfaces, and screening of the dielectric within the material. But calculated optical constants are not sufficient to establish photovoltaic efficiency: absorption spectrum, carrier effective masses, defect formation, charge-carrier recombination, band-edge alignment, and device configuration must also be investigated to determine if $Ag_2SrTiSe_4$ is practical for photovoltaic applications.

Figure 4 shows the calculated optical properties of $Ag_2SrTiSe_4$ over the photon energy range 0–10 eV (real and imaginary parts of the dielectric function, refractive index, extinction coefficient, and absorption coefficient). Optical parameters describe how electromagnetic radiation interacts with material and contain information about electronic polarization, light propagation, and optical absorption. The absorption onset at 2.188 eV means interband optical transitions start in the visible region, while pronounced spectral features at higher photon energies indicate stronger electron excitation. These characteristics are important for possible applications of $Ag_2SrTiSe_4$ as photovoltaic absorbers, ultraviolet photodetectors, optical coatings, and wavelength-selective optoelectronic devices.

Figure 4a shows the real part of $\varepsilon_1(\omega)$, which describes how a material responds to an applied electromagnetic field. The static dielectric constant $\varepsilon_1(0) = 5.2$ means that electrons are polarized at low frequencies. For increasing photon energy $\varepsilon_1(\omega)$ increases monotonically (broad maximum around 9.6 at 4.4 eV) and then drops beyond that energy to about 1.6–2.3 towards the upper end of the investigated energy range due to the energy dependence of the response of electrons to incident radiation and interband electronic transitions. This behavior results from both the energy dependence of electron response to incident radiation and contribution from interband electronic transitions. The enhanced dielectric response around 4.4 eV means a region of pronounced optical dispersion that may influence EM-field distribution, reflection, and confinement in device structures (multilayer optical coatings and wavelength-selective photonic components). These properties are also important for multilayer absorption-loss materials, but absorption losses must be considered as well.

Figure 4b shows the imaginary part of the dielectric function, $\varepsilon_2(\omega)$, the absorptive component of the electronic optical response. Below the optical threshold energy of 2.188 eV, there is no interband absorption in the optical approximation used here; above this energy, $\varepsilon_2(\omega)$ increases as more electronic transitions are accessible, and a maximum of about 8.9 near 4.6 eV (wavelength 270 nm) appears. Other features appear between 5.5 and 6.5 eV, where large optical transitions occur in the ultraviolet region. The strong dielectric absorption at 4.6 eV suggests $Ag_2SrTiSe_4$ could be relevant for UV-sensitive optoelectronic devices. We can investigate the microscopic origin of these absorption features by correlating the dielectric spectrum with band structure, projected density of states, and optical transition matrix elements. In particular, contributions from Ag 4d, Se 4p, and Ti 3d orbitals near the band edges may help explain the electronic transitions responsible for the observed optical response.

The refractive index $n(\omega)$ (Figure 4c) starts from $n(0) = 2.28$ and increases up to about 3.4–3.5 near 4.3 eV, then falls to about 1.4–1.5 above 8 eV. The static value is equal to the electronic dielectric constant through $n(0) \approx \sqrt{\varepsilon_1(0)} = \sqrt{5.2} \approx 2.28$ (assuming nonmagnetic, nonabsorbing low-frequency response). Strong dispersion can support wavelength-selective interference structures and optical interface engineering. Still, a high refractive index is not, by itself, evidence of low-loss waveguiding, since strong absorption may also accompany an enhanced refractive response.

In Figure 4d, $k(\omega)$ and $\alpha(\omega)$ are compared: both are zero below the low-energy cutoff in the ideal response shown but increase above the indicated threshold; the extinction coefficient peaks near 1.7–1.8 around 4.6 eV and the absorption coefficient (roughly) is (6–7) $\times 10^5$ cm^{-1} in a similar region. $\alpha = 4\pi k/\lambda$ links these two quantities (where λ is the vacuum wavelength). For example, $\alpha = 6 \times 10^5$ cm^{-1} gives an intensity-decay length of $1/\alpha \approx 17$ nm, showing how efficiently high-energy photons can be attenuated in thin layers. However, absorption efficiency also depends on surface-reflectance interference and film thickness.

© Ariston Publications 2026. All rights reserved.

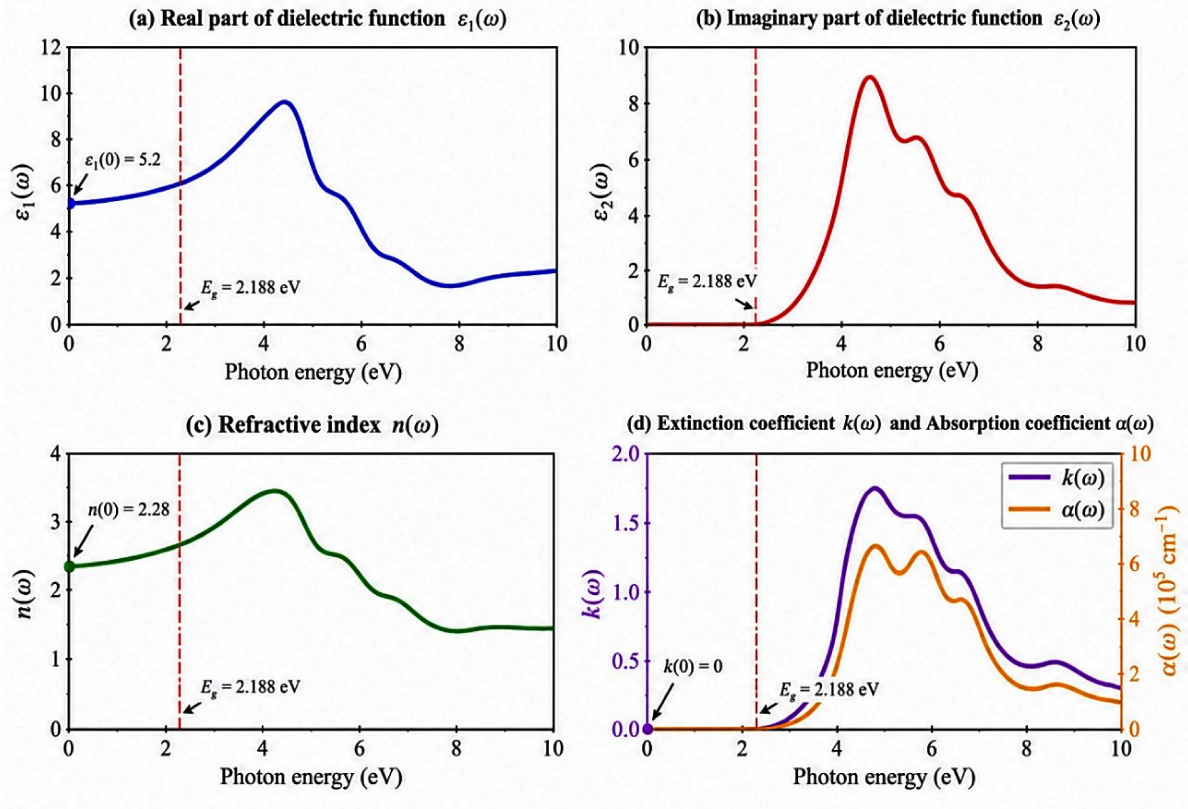

Fig. 4. Photon-energy-dependent optical response of $Ag_2SrTiSe_4$: (a) real part of the dielectric function, $\varepsilon_1(\omega)$; (b) imaginary part of the dielectric function, $\varepsilon_2(\omega)$; (c) refractive index, $n(\omega)$; and (d) extinction coefficient, $k(\omega)$, and absorption coefficient, $\alpha(\omega)$..

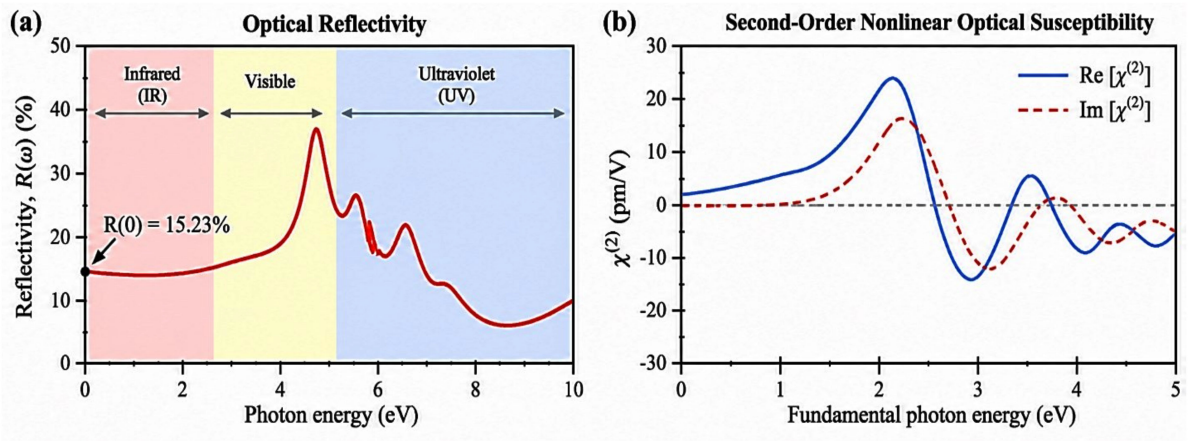

Fig. 5. Photon-energy-dependent linear and nonlinear optical responses of $Ag_2SrTiSe_4$: (a) optical reflectivity, $R(\omega)$, across the infrared, visible, and ultraviolet regions; (b) real and imaginary components of the second-order nonlinear optical susceptibility, $\chi^{(2)}(-2\omega;\omega,\omega)$.

For PV applications, the 2.188 eV optical threshold is about 567 nm, so the nominal onset is visible. This gap could be used for tandem studies of $Ag_2SrTiSe_4$ or other wavelength selective photovoltaic architectures (junctions with a higher energy absorber). Most absorption features in the figure are above threshold (UV mostly). Strong UV absorption does not guarantee broadband solar-harvesting efficiency—to quantify it, you need full solar-spectrum-weighted absorptance, realistic film thicknesses, and carrier-collection properties too.

The spectra also suggest UV photodetectors and optical sensing applications: strong absorption in 4–7 eV might catch UV photons; dispersive refractive response could inform optical-coating design. Responsivity, dark current, detectivity, and speed depend on more than optical constants

© Ariston Publications 2026. All rights reserved.

(defects too, mobility, lifetime, contacts). Figure 4 provides a useful framework for optical response but should be checked for applicability to devices with independently verified spectra and transport data.

In Figure 5, we show the linear and nonlinear optical properties of the quaternary chalcogenide $Ag_2SrTiSe_4$. Reflectivity R(ω) is the fraction of incident optical intensity reflected at an interface; second-order nonlinear susceptibility $\chi^{(2)}$ is polarization induced quadratically by an applied optical field. Together, these quantities provide a useful basis for designing wavelength-selective coatings, optical resonators, integrated waveguides, and nonlinear frequency-conversion components.

In Figure 5a, reflectivity is shown over photon energies of 0–10 eV: at zero photon energy, the plotted reflectivity (15.23%) comes directly from the static refractive index n(0) = 2.28 and extinction coefficient k(0) = 0 (normal-incidence Fresnel expression $R = [(n - 1)^2 + k^2]/[(n + 1)^2 + k^2]$) [60]. The low-energy part of the spectrum in the illustrated plot stays near 14–15%, indicating moderate index mismatch at an ideal air–material interface, but low reflectivity does not mean low propagation loss: waveguide suitability also depends on absorption, scattering, fabrication quality, and the refractive indices of surrounding layers.

Figure 5a shows the photon energy-dependent optical reflectivity of $Ag_2SrTiSe_4$. It increases with photon energy and peaks at about 37% at 4.7 eV; two more peaks appear near 5.5 and 6.5 eV (about 26% and 22%, respectively). Below these peaks, it decreases slowly (about 6% in the range 8.5–9.0 eV). Strong variation in reflectivity implies wavelength dependence of the optical response (especially in the ultraviolet); enhanced reflection near 4.7 eV is due to strong electronic transitions that change the dielectric response. These properties suggest applications as UV reflectors, wavelength-selective optical filters, or multilayer photonic coatings, but increased reflectivity in regions of strong interband transitions may also be accompanied by considerable absorption, so device performance should be considered when assessing such applications.

Figure 5b shows the real and imaginary components of χ^2 (- 2ω; ω, ω) in energy for the fundamental photon energy range 0–5 eV. The plotted real component starts at ∼2 pm/V in the static limit and increases with photon energy up to a positive maximum of nearly 24 pm/V around 2.2 eV. The imaginary component has a strong positive peak of about 16 pm/V near 2.3 eV. At higher photon energies, both components change sign and reach negative minima of −14 and −12 pm/V around 3.0 eV, respectively. At higher photon energies, amplitudes decrease, and smaller oscillations appear in both spectra.

These sharp spectral changes arise from resonant terms in the nonlinear optical response and electronic polarization changes induced by the incident electromagnetic field. These features are important for second-harmonic generation and frequency-conversion applications. However, the quoted peak values are only rough estimates from the plotted curves and should not be used as established nonlinear coefficients of $Ag_2SrTiSe_4$ without symmetry-resolved susceptibility calculations. Quantitative interpretation also requires identifying the corresponding tensor components and checking the susceptibility unit convention.

$Ag_2SrTiSe_4$ belongs to the non-centrosymmetric space group I-42m, whose symmetry allows certain second-order nonlinear optical tensor components (second harmonic generation is, in principle, symmetry-allowed). A fundamental photon energy of 2.2 eV gives a wavelength of about 564 nm, and its second harmonic is about 282 nm (in the UV). This wavelength conversion enables UV generation and research on compact nonlinear photonic components, but $\chi^{(2)}$ amplitude alone cannot tell us whether conversion efficiency is high or low: phase matching, tensor orientation, absorption at both wavelengths, damage threshold, etc., all play roles. So, Figure 5 suggests a combined study of linear optical interface engineering and second-order nonlinear frequency conversion in $Ag_2SrTiSe_4$.

4. CONCLUSION

In this work, we studied the structural, electronic, bonding, and optical properties of the quaternary chalcogenide $Ag_2SrTiSe_4$ using density functional theory to assess its suitability for advanced photonic and optoelectronic devices. This combined analysis helps us understand how atomic arrangement influences orbital contributions to electronic energy levels, optical polarization, and wavelength-dependent electromagnetic interactions, and identifies material characteristics important for optical coatings, UV photodetection, photonic waveguides, and nonlinear frequency conversion technologies. The tetragonal $Ag_2SrTiSe_4$ structure proposed here belongs to space group I-42m. It has an equilibrium unit cell volume of about 410 $Å^3$ and a bulk modulus of 51 GPa (structural parameters of the equilibrium model and hydrostatic compression resistance). Inversion symmetry is not important for nonlinear photonics because electric-dipole second-order optical susceptibility components exist, but quantitative nonlinear coefficients and frequency-conversion performance

© Ariston Publications 2026. All rights reserved.

must be established. The electronic band-structure calculations predict indirect semiconductor behavior with bandgaps of 1.80 eV and 2.50 eV for PBE and HSE$_o$6, respectively. The difference between these values shows how sensitive the predicted electronic structure is to exchange–correlation treatment. Projected density of states show that Ag 4d and Se 4p dominate the valence region. In contrast, Ti 3d states contribute significantly to the conduction region (orbital characteristics may be an electronic basis for interband optical transitions). Electron localization function analysis further shows nonuniform spatial distribution of electron localization around atoms. Based on the optical response reported here, the nominal absorption threshold is 2.188 eV (567 nm). The static refractive index of 2.28 and electronic dielectric constant of 5.2 are consistent and indicate appreciable electronic polarization. The optical absorption coefficient is (6–7) × 10^5 cm^{-1} in the ultraviolet region, indicating strong interaction with high-energy photons. These characteristics lead us to investigate $Ag_2SrTiSe_4$ as an ultraviolet photodetector, wavelength-selective absorber, and related optoelectronic component. The static optical reflectivity of $Ag_2SrTiSe_4$ is about 15.23% (Figure 4), so most of the incident light is reflected at the material surface even in the low-frequency limit; this value matches the refractive index contrast between the material and air and is important for optical interfaces, antireflection coatings, and multilayer photonic structures — refractive index matching could reduce reflection losses and increase light transmission across interfaces. The change in reflectivity as a function of photon energy also suggests wavelength-selective optical behavior (especially in UV), where sharp reflection peaks may be useful for optical filters or reflective coatings. The non-centrosymmetric crystal structure of $Ag_2SrTiSe_4$ allows second-order nonlinear optical processes (second harmonic generation and optical frequency conversion). Still, their efficiency is limited by the magnitude of the nonlinear susceptibility, phase-matching conditions, optical absorption, and polarization-dependent response. The calculated semiconductor characteristics, refractive index dispersion, and UV absorption suggest that $Ag_2SrTiSe_4$ should be further investigated for multifunctional photonic devices. Its use in frequency conversion devices, ultraviolet photodetectors, and optical coatings depends on evaluation of independent nonlinear susceptibility tensor components, optical anisotropy, phase-matching behavior, and defect-related optical losses. Experimental measurements of crystal structure, absorption spectrum, refractive index, and nonlinear optical response would form an essential basis for judging its suitability for practical photonic devices.

DECLARATIONS

Ethical Approval

We affirm that this manuscript is an original work, has not been previously published, and is not currently under consideration for publication in any other journal or conference proceedings. All authors have reviewed and approved the manuscript, and the order of authoR$_{sh}$ip has been mutually agreed upon.

Funding

There are no funding

Availability of data and material

All of the data obtained or analyzed during this study is included in the report that was submitted.

Conflicts of Interest

The authors declare that they have no financial or personal interests that could have influenced the research and findings presented in this paper. The authors alone are responsible for the content and writing of this article.

Author's Contributions

Dr. Kunjlal Singh, Dr. Ratan Lal Jaiswal, Dr. B. S. Yadav, Dr. Hari Narayan Yadav, and Dr. Shiv Shanker Yadav contributed equally to preparing the manuscript.

REFERENCES

[1] Moss, D. J.; Morandotti, R.; Gaeta, A. L.; Lipson, M., **2013**. New CMOS-Compatible Platforms Based on Silicon Nitride and Hydex for Nonlinear Optics. *Nature Photonics*, 7(8), p.597-607. https://doi.org/10.1038/nphoton.2013.183.

[2] Miller, D. A. B., **2010**. Are Optical Transistors the Logical Next Step?. *Nature Photonics*, 4, p.3-5. https://doi.org/10.1038/nphoton.2009.240.

[3] Srivastava, Abhay P.; Pandey, Brijesh K., **2025**. Evaluating Potential Energy Functions for Binding Energy Calculations in Alkali Halide Solids and Molecular Force

© Ariston Publications 2026. All rights reserved.

Constants. *SciEngg Advances*, 2(3), p.119-125. https://doi.org/10.69626/sea.2025.0119.

[4] Leuthold, J.; Koos, C.; Freude, W., **2010**. Nonlinear Silicon Photonics. *Nature Photonics*, 4, p.535-544. https://doi.org/10.1038/nphoton.2010.185.

[5] Srivastava, A. P.; Singh, A. K.; Srivastava, R., **2026**. Improving the Compression Sequence Enhances the Accuracy of the Equation of State, Leading to More Reliable Predictions of Material Behavior in Scientific and Engineering Applications. *International Journal of Petrochemical Science and Engineering*, 8(1), p.12-20. https://doi.org/10.15406/ipcse.2026.08.00146.

[6] Reed, G. T.; Mashanovich, G.; Gardes, F. Y.; Thomson, D. J., **2010**. Silicon Optical Modulators. *Nature Photonics*, 4, p.518-526. https://doi.org/10.1038/nphoton.2010.179.

[7] Todorov, T. K.; Reuter, K. B.; Mitzi, D. B., **2010**. High-Efficiency Solar Cell with Earth-Abundant Liquid-Processed Absorber. *Advanced Materials*, 22(20), p.E156-E159. https://doi.org/10.1002/adma.200904155.

[8] Mitzi, D. B.; Gunawan, O.; Todorov, T. K.; Wang, K.; Guha, S., **2011**. The Path towards a High-Performance Solution-Processed Kesterite Solar Cell. *Solar Energy Materials and Solar Cells*, 95(6), p.1421-1436. https://doi.org/10.1016/j.solmat.2010.11.028.

[9] Sachin; Pandey, Brijesh Kumar; Jaiswal, Ratan Lal, **2022**. Electrical Conductivity of Semiconducting Nanoparticles. *Physica B: Condensed Matter*, 646, p.414279. https://doi.org/10.1016/j.physb.2022.414279.

[10] Todorov, T.; Mitzi, D. B., **2010**. Direct Liquid Coating of Chalcopyrite Light-Absorbing Layers for Photovoltaic Devices. *European Journal of Inorganic Chemistry*, 2010(1), p.17-28. https://doi.org/10.1002/ejic.200900837.

[11] Chen, S.; Gong, X. G.; Walsh, A.; Wei, S.-H., **2009**. Crystal and Electronic Band Structure of Cu2ZnSnX4 (X = S and Se) Photovoltaic Absorbers: First-Principles Insights. *Applied Physics Letters*, 94, p.041903. https://doi.org/10.1063/1.3074499.

[12] Walsh, A.; Chen, S.; Wei, S.-H.; Gong, X. G., **2012**. Kesterite Thin-Film Solar Cells: Advances in Materials Modeling of Cu2ZnSnS4. *Advanced Energy Materials*, 2(4), p.400-409. https://doi.org/10.1002/aenm.201100630.

[13] Srivastava, A. P.; Pandey, B. K., **2026**. Exploring the Influence of Pressure on the Crystal Structure of the High-Temperature Superconductor La1.85Sr0.15CuO4. *MatSci Express*, 3(1), p.41-53. https://doi.org/10.69626/mse.2026.0041.

[14] Jaiswal, R. L.; Pandey, B. K.; Mishra, D.; Fatma, H., **2021**. Thermophysical Behavior of Nanomaterials with the Change in Size and Shape. *International Journal of Thermodynamics*, 24(1), p.1-7. https://doi.org/10.5541/ijot.869865.

[15] Pandey, Kinjjal; Sadanand; Dakua, Pratap Kumar; Panda, Deepak Kumar; Singh, Pravin Kumar; Pandey, B. K., **2024**. Investigation of Suitable Buffer Layer for PbS-TBAI/PbS-EDT Colloidal Quantum Dot Solar Cell Using SCAPS-1D. *Optik*, 298, p.171593. https://doi.org/10.1016/j.ijleo.2023.171593.

[16] Heyd, J.; Scuseria, G. E.; Ernzerhof, M., **2003**. Hybrid Functionals Based on a Screened Coulomb Potential. *The Journal of Chemical Physics*, 118(18), p.8207-8215. https://doi.org/10.1063/1.1564060.

[17] Singh, S.; Singh, A. P.; Gautam, Y. R.; Srivastava, A. P., **2026**. BaFeO3 for Computer Memory Applications: A First-Principles Study of Ferroelectric Switching and Optical Response. *MatSci Express*, 3(3), p.129-146. https://doi.org/10.69626/mse.2026.0129.

[18] Kresse, G.; Furthmüller, J., **1996**. Efficient Iterative Schemes for Ab Initio Total-Energy Calculations Using a Plane-Wave Basis Set. *Physical Review B*, 54(16), p.11169-11186. https://doi.org/10.1103/PhysRevB.54.11169.

[19] Kresse, G.; Joubert, D., **1999**. From Ultrasoft Pseudopotentials to the Projector Augmented-Wave Method. *Physical Review B*, 59(3), p.1758-1775. https://doi.org/10.1103/PhysRevB.59.1758.

[20] Blöchl, P. E., **1994**. Projector Augmented-Wave Method. *Physical Review B*, 50(24), p.17953-17979. https://doi.org/10.1103/PhysRevB.50.17953.

[21] Monkhorst, H. J.; Pack, J. D., **1976**. Special Points for Brillouin-Zone Integrations. *Physical Review B*, 13(12), p.5188-5192. https://doi.org/10.1103/PhysRevB.13.5188.

 © Ariston Publications 2026. All rights reserved.

[22] Becke, A. D.; Edgecombe, K. E., **1990**. A Simple Measure of Electron Localization in Atomic and Molecular Systems. *The Journal of Chemical Physics*, 92(9), p.5397-5403. https://doi.org/10.1063/1.458517.

[23] Sipe, J. E.; Shkrebtii, A. I., **2000**. Second-Order Optical Response in Semiconductors. *Physical Review B*, 61(8), p.5337-5352. https://doi.org/10.1103/PhysRevB.61.5337.

[24] Aversa, C.; Sipe, J. E., **1995**. Nonlinear Optical Susceptibilities of Semiconductors: Results with a Length-Gauge Analysis. *Physical Review B*, 52(20), p.14636-14645. https://doi.org/10.1103/PhysRevB.52.14636.

[25] Rashkeev, S. N.; Lambrecht, W. R. L.; Segall, B., **1998**. Efficient Ab Initio Method for the Calculation of Frequency-Dependent Second-Order Optical Response in Semiconductors. *Physical Review B*, 57(7), p.3905-3919. https://doi.org/10.1103/PhysRevB.57.3905.

[26] Rashkeev, S. N.; Lambrecht, W. R. L.; Segall, B., **1998**. Second-Harmonic Generation in SiC Polytypes. *Physical Review B*, 57(16), p.9705-9715. https://doi.org/10.1103/PhysRevB.57.9705.

[27] Aspnes, D. E., **1982**. Local-Field Effects and Effective-Medium Theory: A Microscopic Perspective. *American Journal of Physics*, 50(8), p.704-709. https://doi.org/10.1119/1.12734.

[28] Levine, B. F., **1969**. Bond-Charge Calculation of Nonlinear Optical Susceptibilities for Various Crystal Structures. *Physical Review Letters*, 22(15), p.787-790. https://doi.org/10.1103/PhysRevLett.22.787.

[29] Kleinman, D. A., **1962**. Nonlinear Dielectric Polarization in Optical Media. *Physical Review*, 126(6), p.1977-1979. https://doi.org/10.1103/PhysRev.126.1977.

[30] Franken, P. A.; Hill, A. E.; Peters, C. W.; Weinreich, G., **1961**. Generation of Optical Harmonics. *Physical Review Letters*, 7(4), p.118-119. https://doi.org/10.1103/PhysRevLett.7.118.

[31] Nkomo, Duduzile; Ngobe, Bongani; Phasha, Maje; Yamabe-Mitarai, Yoko, **2026**. The SCF Convergence Criteria of the Ab Initio Calculations of Elastic Properties of Single-Crystal B2 ZrPd Phase. *Materials Today: Proceedings*, 120, p.154-164. https://doi.org/10.1016/j.matpr.2023.05.219.

[32] Pathak, Shivesh; López, Ignacio Ema; Lee, Alex J.; Bricker, William P.; Fernández, Rafael López; Lehtola, Susi; Rackers, Joshua A., **2023**. Accurate Hellmann-Feynman Forces from Density Functional Calculations with Augmented Gaussian Basis Sets. *The Journal of Chemical Physics*, 158(1), p.014104. https://doi.org/10.1063/5.0130668.

[33] Mishra, Saurav; Pandey, Brijesh Kumar; Srivastava, Abhay Prakash, **2026**. First-Principles Study of Nickel-Doped Calcium Silicate (Ni:CaSiO3) as a Potential Solid-State Defect Qubit Host Material. *Physica B: Condensed Matter*, 739, p.418964. https://doi.org/10.1016/j.physb.2026.418964.

[34] Roller, Deena; Rappe, Andrew M.; Kronik, Leeor; Hellman, Olle, **2024**. Improving the Precision of Forces in Real-Space Pseudopotential Density Functional Theory. *The Journal of Chemical Physics*, 161(7), p.074113. https://doi.org/10.1063/5.0218715.

[35] Srivastava, A. P.; Pandey, B. K.; Pandey, A. K., **2025**. Introducing an Innovative Exponential-Logarithmic Equation of State for Solids at High Compression: HCP Iron Exemplifies This Groundbreaking Advancement. *National Academy Science Letters*. https://doi.org/10.1007/s40009-025-01726-y.

[36] Srivastava, Abhay P.; Pandey, B. K.; Gupta, A. K.; et al., **2024**. The Relevance of the New Exponential Equation of State for Semiconductors. *Iranian Journal of Science*, 48, p.1067-1074. https://doi.org/10.1007/s40995-024-01657-1.

[37] Srivastava, Abhay P.; Sharma, Pankaj; Pandey, Brijesh K.; Mishra, Alok, **2026**. Multifunctional Properties of BaTiO3 Across the Cubic-Tetragonal Phase Transition: Implications for Ferroelectric and Electronic Applications. *Journal of Inorganic and Organometallic Polymers and Materials*. https://doi.org/10.1007/s10904-026-04390-x.

[38] Maurya, D.; Pandey, B. K.; Srivastava, A. P., **2026**. Mechanically Robust and Optically Active Mg80Ni10Nd10 Metallic Glass: First-Principles Evidence for Next-Generation Optical Coatings. *Optical and Quantum Electronics*, 58, p.28. https://doi.org/10.1007/s11082-025-08615-0.

© Ariston Publications 2026. All rights reserved.

[39] Srivastava, A. P.; Pandey, B. K., **2025**. Ab Initio Design of Zr-Based Bulk Metallic Glass for High-Strength and Optical Coating Applications. *Optical and Quantum Electronics*, 57, p.561. https://doi.org/10.1007/s11082-025-08467-8.

[40] Tindibale, Edward; Mulwa, Winfred M.; Adetunji, Bamidele I., **2024**. Elastic Anisotropy, Mechanical, Lattice Dynamics, and Electronic Properties of MPdZ (M = Hf, Zr, Ti; Z = Sn, Ge, Si): DFT Study. *Computational Condensed Matter*, 39, p.e00904. https://doi.org/10.1016/j.cocom.2024.e00904.

[41] Romao, Carl P.; Donegan, S. P.; Zwanziger, J. W.; White, Mary Anne, **2016**. Relationships between Elastic Anisotropy and Thermal Expansion in A2Mo3O12 Materials. *Physical Chemistry Chemical Physics*, 18(44), p.30652-30661. https://doi.org/10.1039/c6cp06356j.

[42] Amari, S.; Bendaoud, H., **2021**. DFT Calculation of Thermo-Elastic Properties and Phonon Dispersions for Terbium Monopnictides TbN and TbP in Rock Salt Structure. *Computational Condensed Matter*, 29, p.e00596. https://doi.org/10.1016/j.cocom.2021.e00596.

[43] Pandey, V.; Pandey, S. K., **2026**. Computational Methods and Algorithms. *Density Functional Theory*. https://doi.org/10.1007/978-981-95-9745-1$_3$.

[44] Srivastava, Abhay P.; Pandey, Brijesh K., **2025**. Analysis of the Structural and Electronic Properties of TiO2 Under Pressure Using Density Functional Theory and Equation of State. *Computational Condensed Matter*, p.e01076. https://doi.org/10.1016/j.cocom.2025.e01076.

[45] Gupta, S.; Srivastava, A. P.; Pandey, B. K., **2026**. Lanthanum-Induced Electronic Transition in Hydride Perovskites: A First-Principles Study of CsXH3 (X = Sc, Y, La, Ac). *International Journal of Biology and Chemistry*, 19(1). https://doi.org/10.26577/IJBCh202619115.

[46] Wood, E. A., **1951**. Polymorphism in Potassium Niobate, Sodium Niobate, and Other ABO3 Compounds. *Acta Crystallographica*, 4, p.353-362. https://doi.org/10.1107/S0365110X51001112.

[47] Hewat, A. W., **1973**. Cubic-Tetragonal-Orthorhombic-Rhombohedral Ferroelectric Transitions in Perovskite Potassium Niobate: Neutron Powder Profile Refinement of the Structures. *Journal of Physics C: Solid State Physics*, 6, p.2559-2572. https://doi.org/10.1088/0022-3719/6/16/010.

[48] Pruzan, P.; Gourdain, D.; Chervin, J.-C.; Canny, B.; Couzinet, B.; Hanfland, M., **2002**. Equation of State of BaTiO3 and KNbO3 at Room Temperature up to 30 GPa. *Solid State Communications*, 123(1-2), p.21-26. https://doi.org/10.1016/S0038-1098(02)00201-6.

[49] Baranek, P., **2007**. Pressure-Driven Phase Transitions of Ferroelectric KNbO3: A Hybrid Functional Approach. *AIP Conference Proceedings*, 963, p.379-382. https://doi.org/10.1063/1.2836090.

[50] Kalinichev, A. G.; Bass, J. D.; Zha, C. S.; Han, P. D.; Payne, D. A., **1993**. Elastic Properties of Orthorhombic KNbO3 Single Crystals by Brillouin Scattering. *Journal of Applied Physics*, 74(11), p.6603-6608. https://doi.org/10.1063/1.355099.

[51] Beaujean, P.; Sanguinet, L.; Rodriguez, V.; Castet, F.; Champagne, B., **2022**. Multi-State Second-Order Nonlinear Optical Switches Incorporating One to Three Benzazolo-Oxazolidine Units: A Quantum Chemistry Investigation. *Molecules*, 27, p.2770. https://doi.org/10.3390/molecules27092770.

[52] Liu, X.; Yang, Z.; Wang, D.; Cao, H., **2016**. Molecular Structures and Second-Order Nonlinear Optical Properties of Ionic Organic Crystal Materials. *Crystals*, 6, p.158. https://doi.org/10.3390/cryst6120158.

[53] Di Bella, S.; Colombo, A.; Dragonetti, C.; Righetto, S.; Roberto, D., **2018**. Zinc(II) as a Versatile Template for Efficient Dipolar and Octupolar Second-Order Nonlinear Optical Molecular Materials. *Inorganics*, 6, p.133. https://doi.org/10.3390/inorganics6040133.

[54] Hernández Fernández, J. A.; Prieto Palomo, J. A.; Ortega-Toro, R., **2025**. Application of Computational Studies Using Density Functional Theory (DFT) to Evaluate the Catalytic Degradation of Polystyrene. *Polymers*, 17, p.923. https://doi.org/10.3390/polym17070923.

[55] Srivastava, Abhay P.; Pandey, Brijesh K., **2025**. Pressure-Dependent Evolution of Bi2Sr2CaCu2O8+delta: DFT Insights for High-Pressure Superconducting Applications. *Solid State Communications*, 404, p.116112. https://doi.org/10.1016/j.ssc.2025.116112.

 © Ariston Publications 2026. All rights reserved.

[56] Takahashi, O., **2024**. A Computational DFT Study of the Stereoinversion of Succinimide Residues Formed in Proteins and Peptides Catalyzed by a Hydrogen Phosphate Ion: An Unsymmetrical SE1 Mechanism. *Symmetry*, 16, p.1369. https://doi.org/10.3390/sym16101369.

[57] Srivastava, A. P.; Singh, A. K.; Srivastava, R.; et al., **2026**. Enhancing the Properties of the High-Temperature Superconductor EuBa2Cu3O6.6 Using Spin-Polarised Density Functional Theory. *International Journal of Petrochemical Science and Engineering*, 8(1), p.37-42. https://doi.org/10.15406/ipcse.2026.08.00149.

[58] Srivastava, Abhay P.; Pandey, B. K.; Singh, Anod Kumar; Srivastava, Reetesh; Srivastava, Harish Chandra, **2025**. Compare Halide Melting Curves Using the Equation of State and Lindemann's Law for a Comprehensive Analysis. *International Scientific Journal of Engineering and Management*, 4(6). https://doi.org/10.55041/ISJEM04566.

[59] Srivastava, A. Prakash; Pandey, B. Kumar; Singh, A. Kumar; Srivastava, R.; Srivastava, H. Chandra, **2025**. Assessment of Several Equations of State for the Calculation of Thermodynamic Coefficients of Solids. *Physical Chemistry Research*, 13(4), p.669-676. https://doi.org/10.22036/pcr.2025.524577.2685.

[60] Srivastava, A. P.; Pandey, B. K., **2026**. First-Principles Investigation of Agx(Ge25Sb10Se65)100-x Chalcogenide Glasses toward Infrared Photonic and Memory Applications. *Applied Physics A*, 132, p.1139. https://doi.org/10.1007/s00339-026-10329-3.

ARISTON PUBLICATIONS

© Ariston Publications 2026. All rights reserved.